

Bcl10 is associated with actin dynamics at the T cell immune synapse

Kaustubh Wagh^a, Brittany A. Wheatley^b, Maria K. Traver^c, Imran Hussain^c, Brian C. Schaefer^c, Arpita Upadhyaya^{a,b,*}

^a Department of Physics, University of Maryland, College Park, MD 20742, USA

^b Institute for Physical Science and Technology, University of Maryland, College Park, MD 20742, USA

^c Department of Microbiology and Immunology, Uniformed Services University, Bethesda, MD 20814, USA



ARTICLE INFO

Keywords:

Bcl10
T cell activation
Actin dynamics
NF-κB
Immune synapse
TIRF microscopy

ABSTRACT

T cell responses to antigen are initiated by engagement of the T cell receptor (TCR)¹, leading to activation of diverse signaling cascades, including an incompletely defined pathway that triggers rapid remodeling of the actin cytoskeleton. Defects in the control of actin dynamics and organization are associated with several human immunodeficiency diseases, emphasizing the importance of cytoskeletal remodeling in the functioning of the adaptive immune system. Here, we investigate the role of the adaptor protein Bcl10² in the control of actin dynamics. Although Bcl10 is primarily known as a component of the pathway connecting the TCR to activation of the NF-κB³ transcription factor, a few studies have implicated Bcl10 in antigen receptor-dependent control of actin polymerization and F-actin-dependent functional responses. However, the role of Bcl10 in the regulation of cytoskeletal dynamics remains largely undefined. To investigate the contribution of Bcl10 in the regulation of TCR-dependent cytoskeletal dynamics, we monitored actin dynamics at the immune synapse of primary murine CD8 effector T cells. Quantification of these dynamics reveals two distinct temporal phases distinguished by differences in speed and directionality. Our results indicate that effector CD8 T cells lacking Bcl10 display faster actin flows and more dynamic lamellipodia, compared to wild-type cells. These studies define a role for Bcl10 in TCR-dependent actin dynamics, emphasizing that Bcl10 has important cytoskeleton-directed functions that are likely independent of its role in transmission of NF-κB -activating signals.

1. Introduction

T cells are an essential component of the adaptive immune system. The T cell receptor (TCR) is stimulated by cognate peptide bound to the appropriate major histocompatibility complex (MHC) allele on the surface of an antigen-presenting cell. One consequence of TCR engagement by specific antigen is activation of a downstream signaling cascade that results in rapid remodeling of the actin cytoskeleton [1]. TCR interaction with stimulatory peptide-MHC results in the formation of signaling microclusters that consist of various downstream signaling molecules clustered around the cytoplasmic face of the TCR. Targets of TCR activation include the Rho family GTPases, which activate actin nucleation promoting factors (NPFs) such as WAVE2, HS1, and WASP [1–4]. These NPFs in turn activate the Arp2/3 complex, nucleating actin polymerization, leading to large scale rearrangements of the actin cytoskeleton and force generation upon T cell activation [5–8]. The

actin cytoskeleton and myosin motors subsequently assemble into a characteristic annular structure [9–11], which is a defining feature of the activated T cell immune synapse [12,13]. This remodeling of the actin cytoskeleton is a hallmark of the T cell response, leading to the formation of the immune synapse. Dynamic remodeling of the actin cytoskeleton is a tightly regulated and biologically important process. Indeed, defects in actin remodeling are mechanistically involved in several immunodeficiencies, such as Wiskott-Aldrich syndrome (WAS) [6]. Defining the molecular mechanisms that regulate actin organization and dynamics at the immune synapse following TCR activation is, therefore, of fundamental importance. Notably, the mechanisms linking the activation of TCR-initiated signaling pathways to changes in cytoskeletal dynamics remain poorly understood.

B cell lymphoma/leukemia 10 (Bcl10) is a small, ubiquitously expressed adaptor protein consisting of an N-terminal caspase recruitment domain (CARD) and a C-terminal region with no identified consensus

* Corresponding author.

E-mail address: arpitau@umd.edu (A. Upadhyaya).

¹ TCR: T cell receptor

² Bcl10: B cell lymphoma/leukemia 10

³ NF-κB: Nuclear factor kappa-light-chain-enhancer of activated B cells

functional domains or motifs. A large number of T cell studies collectively implicate Bcl10 as a key constituent of a TCR-dependent cytosolic NF- κ B signaling intermediate, referred to as the caspase recruitment domain family member 11 (Card11)-Bcl10-mucosa-associated lymphoid tissue lymphoma translocation gene-1 (Malt1) (CBM) complex [14–16]. In the absence of Bcl10 expression, the CBM complex cannot form, and TCR-induced NF- κ B activation is highly impaired. Consequences include defects in production of the critical T cell autocrine growth factor, interleukin-2 (IL-2), and several additional activation-associated proteins. Bcl10 $^{-/-}$ T cells exhibit poor proliferative responses and defective effector differentiation [17,18]. Defects in CBM complex signaling are also mechanistically associated with a growing list of primary immunodeficiencies [19], further emphasizing the importance of Bcl10 and its partners in normal immune system function.

Interestingly, a few studies have implicated Bcl10 in the regulation of the actin cytoskeleton. In one such study, Rueda et al. [20] showed that, independent of its role in NF- κ B activation, Bcl10 regulates actin organization in Jurkat cells and CD4 $^{+}$ primary murine T cells. Specifically, they identified Ser138 as a critical phosphorylation site that affects F-actin organization but does not impact NF- κ B activation. However, these studies primarily employed biochemical methods, static imaging and functional assays, leaving the role of Bcl10 in the regulation of cytoskeletal dynamics largely unaddressed. Moreover, these studies did not address the potential role of Bcl10 in the regulation of the actin cytoskeleton in CD8 effector T cells (also called cytotoxic T lymphocytes (CTLs)), a subset required for the killing of host cells infected with intracellular pathogens. In this work, we define the role of Bcl10 in regulating cell morphology and actin dynamics in primary murine CD8 effector T cells. We used interference reflection microscopy (IRM) to image cell morphology and total internal reflection fluorescence (TIRF) microscopy to examine actin dynamics with high temporal and spatial resolution in CD8 T cells. Quantification of these dynamics using spatiotemporal image correlation spectroscopy (STICS) reveals two distinct temporal phases. Actin flows are fast and directed inward but rapidly slowing down during the early phase followed by a phase with slower and more steady speeds and more randomly oriented flows. Our data and analyses indicate that cells lacking Bcl10 display more prominent edge dynamics compared to wildtype cells. Our results also demonstrate that lack of Bcl10 leads to faster actin flow speeds at the T cell immune synapse during both temporal phases.

2. Results

2.1. CD8 effector T cells lacking Bcl10 have more dynamic lamellipodia, but normal spreading kinetics

In order to probe the role of Bcl10 in the dynamics and organization of the actin cytoskeleton in primary murine CD8 effector T cells, we purified CD8 T cells from lymph nodes (LN) and spleens of wild type (WT) and Bcl10 $^{-/-}$ mice [17], followed by in vitro differentiation by approximately seven days of expansion in media supplemented with interleukin-2 (IL-2). We confirmed by Western Blot that Bcl10 $^{-/-}$ CD8 T cells do not express Bcl10 but do express its signaling partner Malt1 at the same level as wildtype cells (Supplementary Fig. 1). We have previously shown that Bcl10 $^{-/-}$ CD8 T cells expand and differentiate efficiently when provided with ample anti-TCR/anti-CD28 stimulation and interleukin-2 [18]. To investigate the dynamics of cell morphology and the actin cytoskeleton upon stimulation of these CD8 effectors, we activated WT and Bcl10 $^{-/-}$ cells on an anti-TCR β coated substrate. We then imaged the cells as they responded to TCR activation using interference reflection microscopy (IRM) [21]. Fig. 1a shows a montage of time-lapse images from a representative WT (top panel) and Bcl10 $^{-/-}$ (bottom panel) cell. From the IRM time-lapse movies, we quantified the spreading kinetics of WT and Bcl10 $^{-/-}$ cells. The IRM images were segmented to obtain binary masks in order to quantify the change in the

contact area over time (see Methods). We then fit the spreading area versus time curve to a hyperbolic tangent ($tanh$) function to extract a spreading rate, as shown for four representative WT (black) and Bcl10 $^{-/-}$ (red) cells (Fig. 1b). The spreading curves of all WT cells (N = 34) and Bcl10 $^{-/-}$ cells (N = 35 cells) followed this characteristic pattern and a tanh fit yielded a spreading rate for each cell, similar to our previous results on Jurkat T cells [21]. Comparison of the population spreading rates showed that Bcl10 $^{-/-}$ cells exhibited higher variability compared to WT cells even though the mean spreading rates were not significantly different (Fig. 1c).

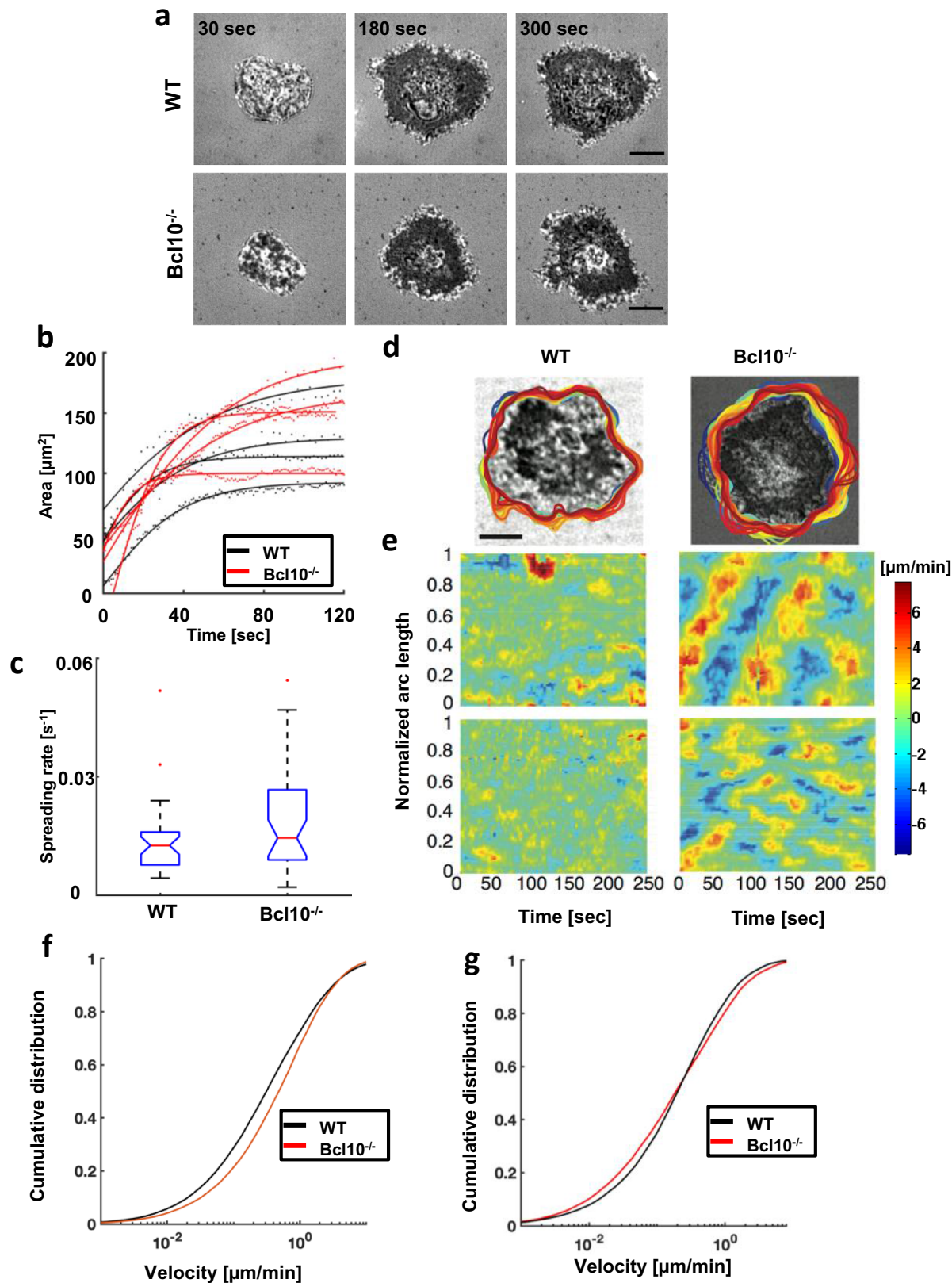
After the initial spreading phase and upon reaching their maximal spread state, cells continue to display significant protrusions and retractions of the cell edge. These morphological dynamics may be indicative of the stability of the immune synapse. From the IRM images of these cells, we extracted the contours and quantified the dynamics of the edges using a level set algorithm to calculate the edge velocities [9,22]. A representative snapshot of each cell type is shown in Fig. 1d. The contours are color coded such that blue contours represent early times and red contours represent late times, while the heatmaps of the edge velocities represent protrusions (red) and retractions (blue) (Fig. 1e). The WT cells show largely disorganized protrusion-retraction patterns while the Bcl10 $^{-/-}$ cells show sustained cycles of protrusions and retractions along the cell periphery that are evident from the diagonal stripes in the heatmaps of edge velocities (2 representative cells are shown for each condition in Fig. 1e). In order to quantify the dynamics of the cell boundary motion, we used a spatiotemporal spectral decomposition method [23]. This method decomposes the protrusion-retraction cycles along the cell edge into a small set of component waveforms called “modes”, using an empirical mode decomposition and the Hilbert-Huang transform (HHT). We restricted our decomposition to a total of five modes to ensure numerical convergence in the calculation of the modes. We also focused our analysis on the later phase of spreading (past the 4 min time point), when the cells were fully extended and clear protraction/retraction dynamics could be observed. We found that the low order modes were broadly distributed in frequency, representing the stochastic dynamics of the cell edge, whereas the higher order modes represented very low frequency cell-wide movements (Supplementary Fig. 2). However, Modes 2 and 3 effectively captured the protrusion-retraction dynamics of the cell edge observed in Fig. 1e. The amplitude distributions of these modes across WT and Bcl10 $^{-/-}$ cells as determined by the HHT differed slightly but significantly, with Bcl10 $^{-/-}$ cells exhibiting overall higher amplitudes, indicative of increased oscillatory dynamics of the cell edge, relative to WT (Fig. 1f, g). Thus, we find that Bcl10 $^{-/-}$ cells display greater variability in their spreading kinetics and more dynamic edges during spreading. Since TCR induced spreading is actin mediated, we conjectured that these differences may be related to actin organization and dynamics at the T cell immune synapse.

2.2. WT and Bcl10 $^{-/-}$ CD8 effector T cells display a highly dynamic actin cytoskeleton

We next examined whether the organization and dynamics of the actin ring was altered in Bcl10 $^{-/-}$ cells. In order to study the dynamics of actin flows at the immune synapse, WT and Bcl10 $^{-/-}$ cells were transduced using a retroviral construct expressing F-tractin-EGFP, a reporter that binds specifically to F-actin [24]. We activated these cells as described above using substrate bound anti-TCR β , and monitored actin dynamics at the synapse using TIRF microscopy. Time-lapse TIRF imaging showed dramatic actin reorganization at the contact zone. For both WT and Bcl10 $^{-/-}$ cells, upon activation by contact with the activating surface, the actin cytoskeleton organized itself into dynamic patterns spreading outwards in multiple ‘fronts’ or ‘waves’ (Movie 1), which may be similar to the actin-membrane waves that correlate with the formation of signaling clusters, as described in earlier work [9,25]. We also observed a characteristic clearance of actin in the cell center

(i.e. formation of an actin ring), which persisted for 1–2 min, followed by recovery of actin over the entire contact zone and a closure of this ring (as shown for both WT and $Bcl10^{-/-}$ cells in Fig. 2a). This actin clearance is concurrent with the secretion of granules by CTLs, as

described before [26]. The later stages of spreading were characterized by dynamic actin foci and a network of filaments in the contact zone (Movie 1), which have been described previously for activated CD4⁺ and Jurkat T cells [27–29]. We found that $Bcl10^{-/-}$ cells also displayed



(caption on next page)

Fig. 1. Spreading and morphological dynamics of activated T cells. (a) Time-lapse interference reflection microscopy (IRM) images of WT (top panels) and $Bcl10^{-/-}$ (bottom panels) primary mouse effector T cell spreading on a stimulatory coverslip coated with anti-TCR β antibody. Scale bar: 5 μ m. (b) Representative spreading curves for WT (black) and $Bcl10^{-/-}$ (red) cells. Datapoints are marked as dots, and the smooth curves are the $tanh$ fits. (c) Spreading rates of WT ($N = 34$) and $Bcl10^{-/-}$ ($N = 35$) cells. Kolmogorov-Smirnov (K-S) test shows that the variances are significantly different ($p < 0.05$). (d) Cell contours as a function of time for WT (left panels) and $Bcl10^{-/-}$ (right panels). Contour color scheme is in a scale from blue to red with blue contours representing early times and red representing later times. Contours are plotted between 7 and 11 min after spreading initiation, when the cell had maximally spread. Scale bar: 5 μ m. (e) Heatmaps of edge velocities calculated from contours in (d) using a level-set algorithm. The colors correspond to the velocity values as depicted in the color bar. The two left panels are for WT cells and the two right panels are for $Bcl10^{-/-}$ cells. Protrusions are in red and retractions are in blue. (f)–(g) Cumulative distribution function of the amplitude of Modes 2 and 3 respectively from the empirical mode decomposition of edge velocities (calculated between 4 and 11 min of spreading) for a population of WT (black, $N = 7$) and $Bcl10^{-/-}$ (red, $N = 9$) cells. K-S test shows that the distributions are significantly different ($p < 10^{-5}$).

a qualitatively similar behavior of actin clearance followed by recovery (Fig. 2a). The times required for actin recovery in these cells were largely similar, $152 \text{ s} \pm 111 \text{ s}$ seconds for WT ($N = 9$ cells) and $128 \text{ s} \pm 58 \text{ s}$ for $Bcl10^{-/-}$ ($N = 16$ cells).

The formation and closure of the actin ring and the morphological changes in CTLs suggests extensive lamellipodial actin dynamics during T cell activation which we hypothesized may be modulated by $Bcl10$ signaling. In order to further characterize these dynamics, we obtained TIRF images of F-tractin-EGFP labeled actin in these cells (Fig. 2b) with high temporal resolution (1 s time interval between frames). To quantify actin flows, we used Spatiotemporal Image Correlation Spectroscopy (STICS) [30], which is a technique that incorporates fluorescence intensity correlations across spatial and temporal interrogation windows in order to quantify changes in protein dynamics over space and time. An illustrative example from STICS analysis is shown in Fig. 2c. The resulting velocity vectors can be analyzed in terms of their magnitudes (lengths of the arrows in Fig. 2c) and their directions (Fig. 2c inset), both of which show temporal evolution. To better study their time dependence, we decomposed the velocity vectors resulting from the STICS analysis into heatmaps of speeds or magnitudes (Fig. 2d) and directional coherence of velocity vectors as described in Methods (Fig. 2e). Higher speeds correspond to yellows while lower speeds correspond to blues in the representative speed heatmap (Fig. 2d). Qualitatively, we observe an initial (early) phase of higher speeds distributed peripherally (yellows in the first panel of Fig. 2d), while the later stages show a decrease in flow speeds (more blues in the heatmap). From the directional coherence heatmaps, we see an early stage of distinct inward directed peripheral flows (preponderance of yellows in Fig. 2e, leftmost panel). Thus, both WT and $Bcl10^{-/-}$ CD8 T cells display a highly dynamic actin cytoskeleton, with both genotypes showing the characteristic clearance and recovery of actin from the contact zone. STICS analysis on WT cells indicates the presence of two qualitatively different temporal phases in actin dynamics.

2.3. Spatiotemporal image correlation spectroscopy (STICS) reveals the existence of novel temporal behavior of actin dynamics in CD8 effector T cells

In order to compare the actin dynamics between WT and $Bcl10^{-/-}$ cohorts, we sought to first quantify the temporal behavior of actin flows in WT cells. Fig. 3a shows the temporal evolution of the probability density function (PDF) of actin flow speeds over time, with blues indicating early times, and yellows indicating later times. We observe that the distribution narrows and shifts leftward over time, indicating that the speeds are slower and more tightly distributed at later times. To quantify the temporal evolution of the PDF, we tracked the system in the phase space of the mean and standard deviation of the PDF of flow speeds. Fig. 3b shows a scatterplot of mean speed (x-axis) and the standard deviation (y-axis) of the PDF's. The scatterplot is color coded so that blues indicate early times while yellows indicate later times. As anticipated, the temporal evolution of the system follows an almost monotonic decrease in both the mean and standard deviation of the PDF, until it gets trapped in the lower left region of the phase space (Fig. 3b). We then used a k-means clustering approach [31] to classify the scatterplot into two distinct clusters (Fig. 3c). A k-means

classification can classify any set of datapoints into an arbitrary number of clusters. We choose to classify the data into two clusters because we qualitatively observed that the actin dynamics show two distinct types of behavior (Fig. 2d, 2e). Fig. 3d shows a plot of the mean actin flow speed over time for the same representative cell as in Fig. 3a–c. The shaded error bars indicate $2.576 \times \text{SEM}$, which for a normally distributed dataset, would correspond to the 99% confidence interval; in this case, it serves as a measure of the spread in the data. The colors correspond to the state assignment obtained from the k-means clustering shown in Fig. 3c. We find that these state assignments correspond to two distinct phases: Phase 1 (blue) consists of higher but rapidly decreasing speeds, and Phase 2 (orange) consists of slower but more stable speeds (Fig. 3d).

For the rest of the analysis, we divided all the flows into these two phases, which were determined separately for each cell by the same unbiased clustering approach. From the spatial distribution of the directional flow vectors, we defined a metric called the second spatial moment (SSM) to quantify the spatial distribution of inward flows. A higher SSM indicates a more peripheral distribution of inward flows, while a lower SSM indicates either a more centrally clustered or a more randomized distribution of flows (see Methods). The two phases we defined using the mean flow speed also shows a natural division for the SSM: a reduction in the mean flow speed coincides with a reduction in the SSM. We found that the SSM decreases in the early stages during Phase 1 and becomes roughly constant at later times in Phase 2 (Fig. 3e). This lower SSM at late stages is indicative of a more random distribution of flow directions concurrent with an overall decrease in the flow speeds. These observations indicate that actin forms a ring of fast, centripetal flows at early times, which become disorganized, and disintegrate into more incoherent flows at later times.

In order to compare the speeds and directions for the entire population of cells studied, we constructed the cumulative distribution function (CDF) of the flow speeds from all the velocity vectors of all cells, after binning the data into the two temporal phases as defined above. As expected, the CDF for the actin flow speeds is shifted to the right for Phase 1 as compared to that for Phase 2 (Fig. 3f). This rightward shift indicates that, at the population level, the distribution of flows is faster in Phase 1 than in Phase 2. We also constructed the probability density function (PDF) for the directional coherence (Fig. 3g). The directional coherence in Phase 1 (blue curve) shows a larger proportion of inward flows (defined as directional coherence larger than 0.8) than that for Phase 2 (orange curve), as shown in Fig. 3g (inset). This observation indicates that actin retrograde flows are enhanced in the early spreading phase than in the later phase. We similarly compared the SSM of inward flow of each phase and found that the SSM in Phase 1 is higher than that in Phase 2, indicating more peripheral flows in Phase 1, and more randomly oriented flows in Phase 2 (Fig. 3h). These data, together with the PDF of directional coherence implies that not only is there a higher proportion of inward flow in Phase 1, but also that the distribution of these flows is more peripheral in Phase 1 than in Phase 2. This finding is consistent with our observation of a band of retrograde flow in the lamellipodial and lamellar regions. This phenomenon has also been described in the context of Jurkat T cells spreading on stimulatory planar lipid bilayers [32], suggesting that this dynamic behavior may be a general feature of actin

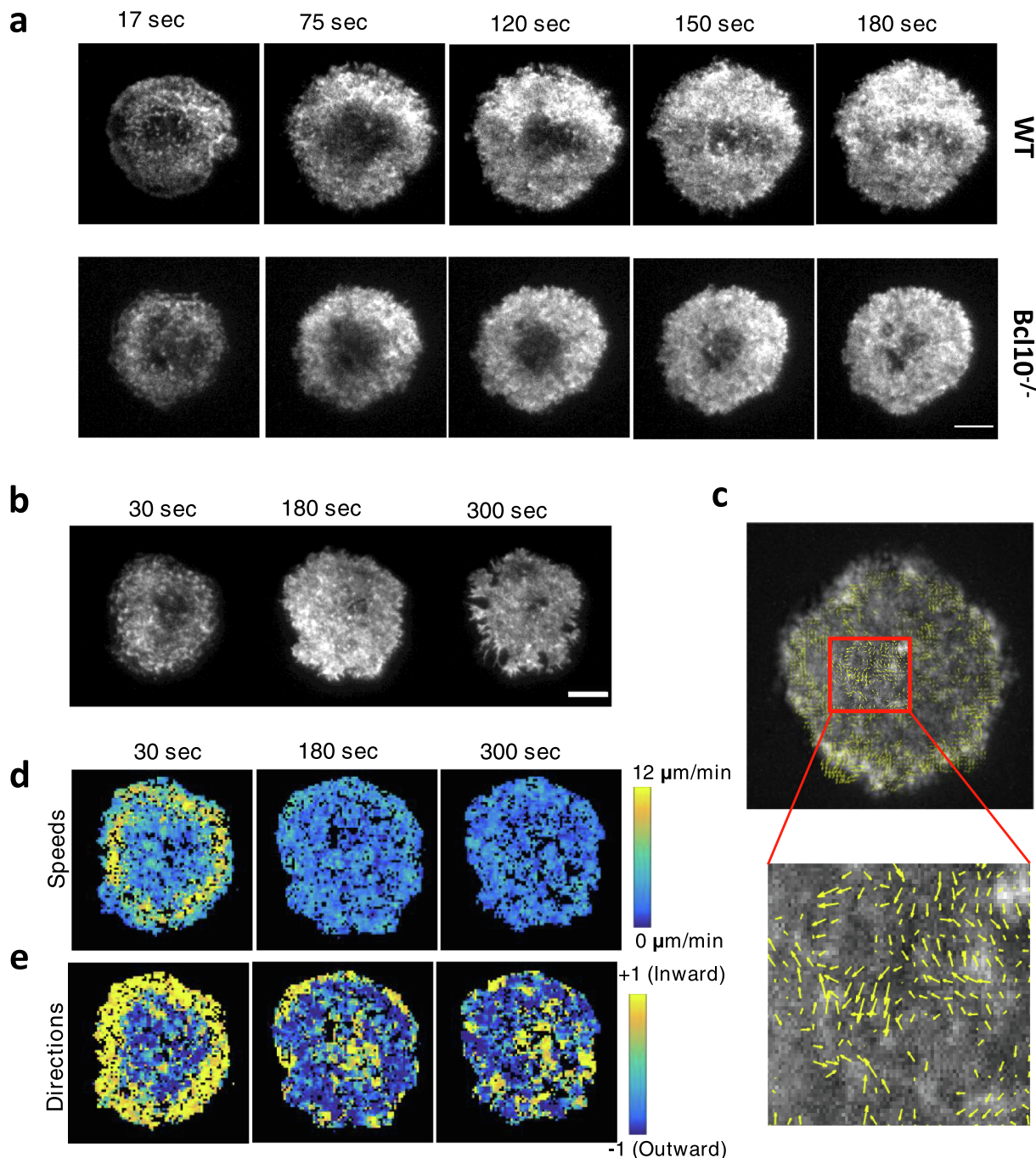


Fig. 2. Analysis of actin dynamics reveals qualitative temporal differences in actin flows (a) Time-lapse TIRF images of F-tractin-EGFP labeled CD8 T cells spreading on a stimulatory glass coverslip (top panels: WT cells, bottom panels: Bcl10^{-/-} cells) showing the clearance of actin in the central region following subsequent recovery of actin in the entire contact zone. (b) Time-lapse montage of a WT CD8 primary mouse effector T cell expressing F-tractin-EGFP spreading on a stimulatory glass coverslip coated with anti-TCR β antibody. Scale bar: 5 μ m. (c) Spatiotemporal image correlation spectroscopy (STICS) analysis illustrating the spatiotemporal behavior of actin flows at the immune synapse. Yellow arrows corresponding to velocity vectors over a region of interest are superimposed on a TIRF snapshot (left panel). The lower panel shows a zoomed in view of the area enclosed by the red box. (d) Spatial heat map showing the magnitudes of actin flows speeds at three time points. Colors correspond to the speed as indicated in the color bar. (e) Spatial heat map showing the directional coherence of actin flows at three time points. Colormap is on a scale such that blue indicates flows away from the center and yellow indicates flows towards the center.

flows in TCR-stimulated T cells.

2.4. Bcl10 modulates actin dynamics in CD8 effector T cells

We next examined actin flows in Bcl10^{-/-} CD8 effector T cells and compared these to our results from WT cells. Fig. 4a shows a representative montage of time-lapse images of spreading F-tractin-EGFP-expressing Bcl10^{-/-} T cells. As with WT cells, we used STICS analysis

to obtain flow speeds and directional coherence values as shown in the spatial heatmaps (Fig. 4b, c). The actin flow speeds in Bcl10^{-/-} T cells also exhibit two phases with a faster initial phase and slower late phase, as observed with WT cells. We then applied our classification scheme to compare the actin dynamics in WT and Bcl10^{-/-} cells. We found that actin flows were significantly faster in Bcl10^{-/-} cells as compared to those in WT cells in both phases of activation (Fig. 4d). Similar to WT cells, the directional coherence in Phase 1 for Bcl10^{-/-} (blue dashed

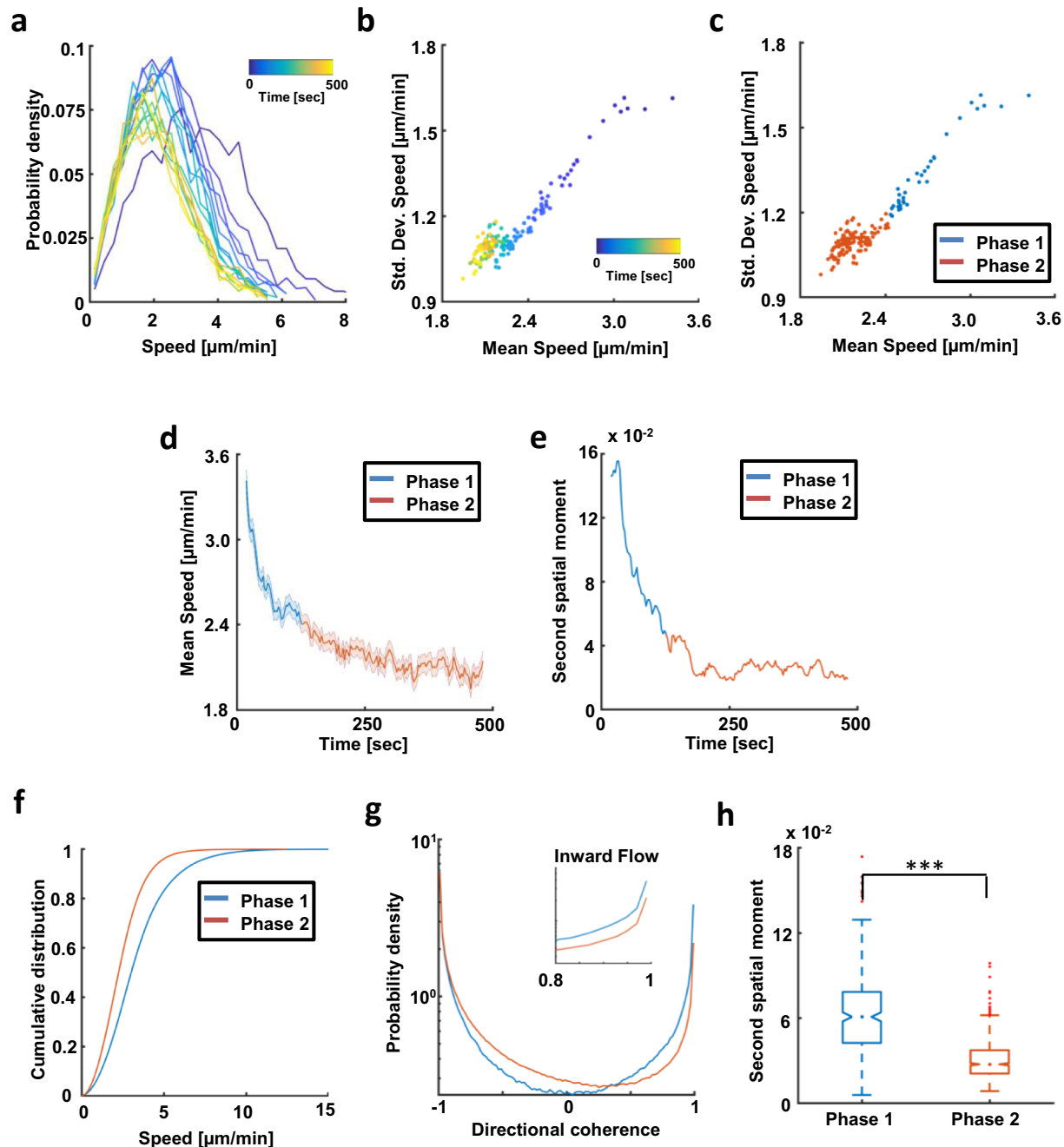


Fig. 3. Temporal dynamics of actin flows during T cell activation. (a)-(e) Panels show results for one representative cell (a) Probability density functions of speeds obtained from STICS plotted for several sample times. Blues indicate early times and yellows indicate later times. (b) Scatter plot of mean and standard deviation of the distributions of speeds. Blues indicate early times and yellows indicate later times. (c) Results of k-means clustering into two clusters. (d) Mean speed as a function of time, color-coded according to the clusters identified in (c). Shaded error bars indicate $2.576 \times$ standard error. (e) The second spatial moment (SSM) of inward flows of the same cell as in (a)-(d) plotted as a function of time. The SSM is used to quantify the spatial distribution of inward flows (i.e. directional coherence greater than 0.8). (f) The cumulative distribution function of actin flow speeds obtained from STICS analysis for WT cells ($N = 12$ cells). Flow speeds in Phase 1 (blue line) are higher than those in Phase 2 (orange line), as indicated by a leftward shift in the CDF for Phase 2. These distributions are significantly different ($p < 10^{-53}$, K-S test). (g) The probability density function of directional coherence obtained from STICS analysis for WT cells (Phase 1 in blue, and Phase 2 in orange). Inset shows that flows in Phase 1 (blue) display a higher probability of inward (retrograde) flow than those in Phase 2 (orange). ($p < 3 \times 10^{-6}$ proportions test). (h) Boxplot of second spatial moment (SSM) of inward flow for Phase 1 (blue) and Phase 2 (orange) (***) $p < 10^{-71}$, Mann-Whitney U test, $N = 12$ cells).

curve) shows a larger proportion of inward flows (directional coherence larger than 0.8) than that for Phase 2 (orange dashed curve), as shown in Fig. 4e. The directional coherence values were not significantly different between $Bcl10^{-/-}$ and WT cells in either temporal phase. We then compared the SSM of inward flow in each phase for WT and $Bcl10^{-/-}$ cells and found that it was lower in Phase 2 than in Phase 1 for each cell type (Fig. 4f). Interestingly, the SSM showed a significant

difference between $Bcl10^{-/-}$ and WT cells for each phase, however the spread in the data is quite large, so these differences are not as robust as the differences in speed. The cumulative distribution functions for the SSM for each cell type in Phase 1 (Fig. 4g) and Phase 2 (Fig. 4h) illustrate these differences in the SSM. We speculate that these differences in the spatial structure of retrograde flow are important for T cell activation, and for maintaining the stability of the immune synapse.

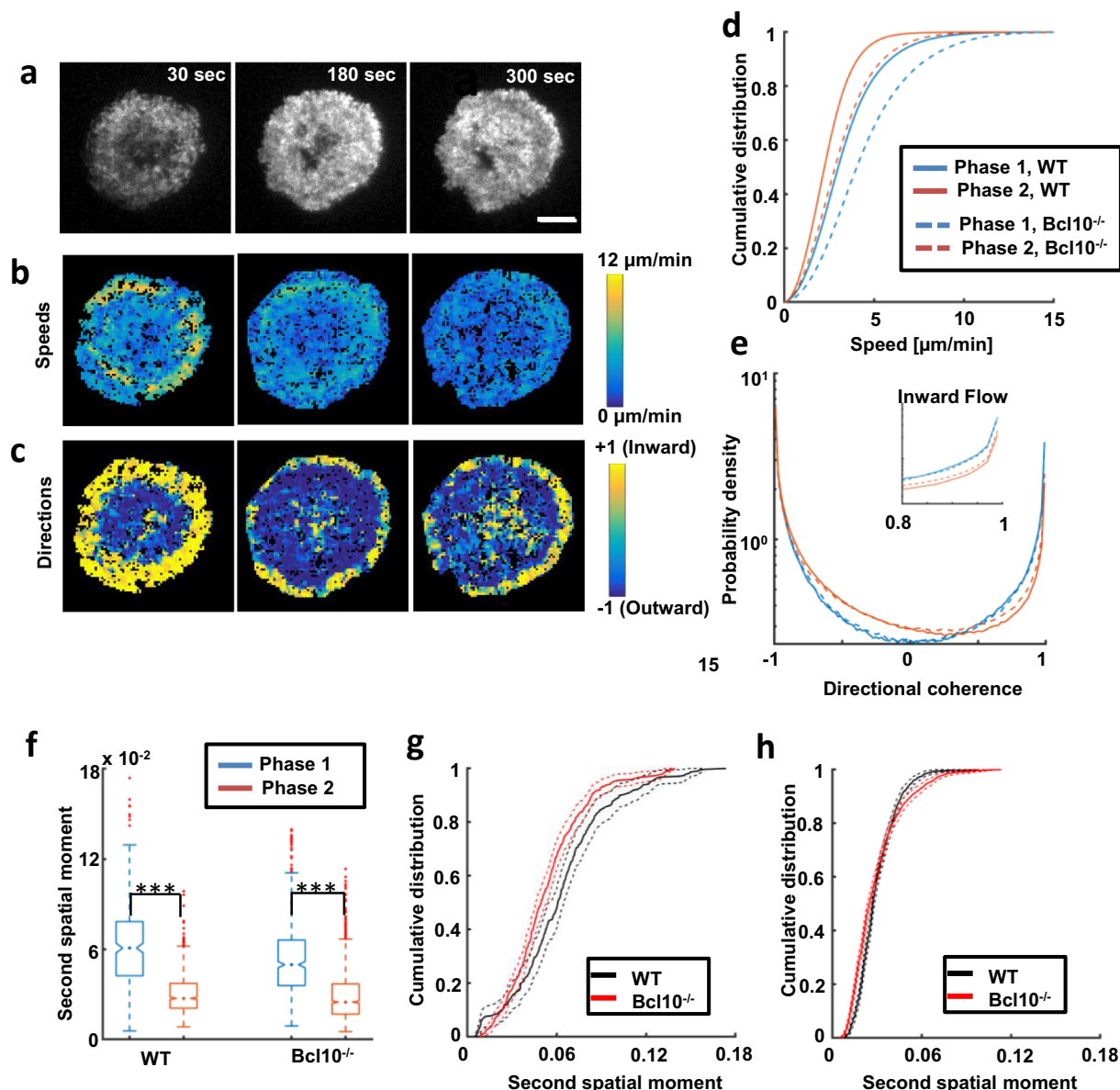


Fig. 4. Bcl10^{-/-} cells display higher actin flow speeds compared to WT cells (a) Time-lapse images of a Bcl10^{-/-} primary mouse effector T cell expressing F-tractin-EGFP spreading on a stimulatory glass coverslip coated with anti-TCR β antibody. Scale bar: 5 µm. (b) Time-lapse montage of heatmaps of flow speeds obtained from STICS analysis at three time points for a representative Bcl10^{-/-} cell. The colors correspond to speeds as indicated in the colorbar. (c) Time-lapse montage of heatmaps of directional coherence from STICS analysis at the same three time points for the same cells. The colors correspond to inward (yellow) and outward (blue) flows. (d) Comparison of cumulative distribution function of actin flow speeds in WT (solid lines) and Bcl10^{-/-} (dashed lines) cells, with Phase 1 flows in blue and Phase 2 flows in orange. ($p < 10^{-27}$, Kolmogorov-Smirnov test, N = 12 WT and N = 21 Bcl10^{-/-}). (e) Probability density of directional coherence for WT (solid lines) and Bcl10^{-/-} (dashed lines) cells shows no significant difference. Within each condition, the proportion of inward flow is higher in Phase 1 (blue) than in Phase 2 (orange) ($p < 10^{-5}$, proportions test). (f) Boxplots of second spatial moment of inward flow for WT and Bcl10-KO in the two different phases (Phase 1 in blue, Phase 2 in orange) (***) $p < 10^{-72}$ Mann Whitney U Test. (g)-(h) Cumulative distribution functions for the second spatial moment of inward flows plotted for Phase 1 (g) and Phase 2 (h). Black lines represent quantification for WT cells, while red lines represent that for Bcl10^{-/-} cells. Solid lines indicate the empirical CDF, while dotted lines indicate the 99% confidence intervals.

Our results show that similar to WT cells, Bcl10^{-/-} cells show faster inward directed actin flows in the early phase, and slower randomly directed flows in the later phase of activation. Importantly, lack of Bcl10 expression leads to faster actin flows during both early and late phases of cell activation, as compared to WT cells. This result indicates that Bcl10 may be important in regulating actin assembly and dynamics to maintain optimum actin flows at the immune synapse.

3. Discussion

In this study, we have used a variety of live cell imaging approaches

to define novel connections between the adaptor molecule Bcl10, and TCR-dependent regulation of actin cytoskeletal dynamics in CD8 effector T cells. Interestingly, although both WT and Bcl10^{-/-} T cells formed actin rings in a similar manner, the distribution of spreading rates in Bcl10^{-/-} CD8 T cells was significantly different from that for WT cells. Also, the two cell types exhibited distinct protrusion-retraction dynamics at the periphery of the zone of contact with the TCR-stimulating substrate. To determine whether these morphological differences were correlated with differences in cytoskeletal dynamics between WT and Bcl10^{-/-} CD8 effector T cells, we used spatiotemporal image correlation spectroscopy (STICS) analysis to measure actin flows

at the cell-substrate boundary during TCR activation. Using this methodology, we initially defined two distinct phases of actin flows in WT CD8 effector T cells. The first phase occurs during approximately the first two to three minutes of spreading, during which actin flow speeds are rapidly decreasing with flows being preferentially oriented toward the center. Immediately following this early phase, there is a distinct second phase, characterized by reduced and relatively constant actin flow speeds, but with more randomly oriented actin flow directions. We then compared the behavior of WT and $Bcl10^{-/-}$ T cells, which revealed that actin flow speeds are substantially accelerated in $Bcl10^{-/-}$ T cells during both phases, whereas the directional coherence is indistinguishable from that in WT cells.

Taken together, our data show that while the absence of $Bcl10$ has a significant impact on a subset of parameters of TCR-dependent actin dynamics, other parameters are not impacted, relative to the behavior of WT cells. These selective defects thus suggest that $Bcl10$ is mechanistically involved in the control of a process or pathway that regulates specific aspects of actin dynamics, rather than being a signal transducer that lies upstream of all TCR-dependent signaling to the actin cytoskeleton. More specifically, our data are consistent with $Bcl10$ controlling an actin remodeling process that determines flow rates, without having a clear impact on F-actin distribution and directional coherence.

We note that our observation of two temporal phases of actin dynamics in primary T cells is unique compared to prior work which described two spatial components of actin flows corresponding to distance from the cell periphery in Jurkat T cells [10]. Our qualitative observation of a distinct band of inward directed faster flows in the early phase of spreading suggests an underlying spatial organization worth exploring. The difference in actin dynamics may have a significant effect on signaling and cytolytic function through the development of differential forces across engaged TCR/ligand clusters as well as integrins in these different phases. In related recent work, we have shown that actin dynamics directly modulate B cell receptor mobility and signaling [33], raising the possibility that T cell receptor signaling may also be regulated by dynamic actin networks. Our finding of differential actin flows over time indicates the need for future studies of time evolution of actin dynamics and their effect on signaling (e.g. microcluster formation) and effector function (e.g. regulation of granule secretion in CD8 cells). Our current studies with TIRF do not have sufficient spatial resolution to visualize the formin-nucleated actomyosin arcs that have been described previously with super-resolution imaging in both Jurkat and primary T cells [11]. While it is likely that $Bcl10$ also modulates the dynamics of arcs, future work with super-resolution imaging of myosin and actin will enable us to compare dynamics across spatial regions and examine the role of $Bcl10$ on myosin, formin, and these distinct actin architectures. Previous studies have published data showing that upon TCR engagement, $Bcl10$ is recruited to the immune synapse along with its signaling partner Card11 [34,35]. Simultaneous imaging of $Bcl10$ and actin and actin-regulatory proteins would be informative to further probe direct interactions between the two proteins.

To our knowledge, only two previous studies have investigated connections between $Bcl10$ and antigen receptor-dependent actin remodeling. In the earliest publication to address this topic, Rueda et al. [20] showed that $Bcl10$ deficiency in Jurkat T cells (by shRNA silencing) and primary murine naïve T cells (by germline gene inactivation) have a reduced F-actin content in response to stimulation with soluble anti-CD3. Additional experiments with $Bcl10$ -silenced Jurkat T cells showed that spreading on a glass substrate in response to immobilized anti-CD3 and conjugate formation in response to SEE-presenting Raji cells were deficient. However, their studies were done with fixed cells and population assays, with significant effects observed at a single time point in each type of experiment. Notably, we found that $Bcl10^{-/-}$ CD8 effector T cells do not display a strong defect in cell spreading, in contrast to the spreading defect reported by Rueda et al. However,

primary effector T cells were not examined in that publication and neither naïve T cells nor Jurkat T cells were examined in our work. Due to the above differences in study design, it is therefore difficult to directly compare the results of Rueda et al. with our findings regarding TCR-stimulated F-actin dynamics.

In a later study, Marion et al. [36] investigated the role of $Bcl10$ in actin polymerization and membrane remodeling downstream of stimulation of a distinct antigen receptor, the $Fc\gamma$ receptor ($Fc\gamma R$). Their data showed that $Bcl10$ deficient macrophages have a defect in $Fc\gamma R$ -dependent phagocytosis, due to the formation of actin-rich phagocytic cups that fail to fully extend and close. Furthermore, these defective phagocytic cups had increased N-WASP, Arp3 and Cdc42 accumulation. Based on these observations and additional data, the authors concluded that $Bcl10$ may be important in down-regulating actin assembly via a Rac-mediated pathway, which ultimately allows phagocytic cup closure to proceed to completion. Our data demonstrating TCR-dependent increases in actin dynamics in the absence of $Bcl10$ are roughly consistent with the results reported by Marion et al. However, whether $Bcl10$ regulates a similar or identical Rac-dependent pathway downstream of TCR stimulation remains an open question that will need to be specifically addressed by future investigations.

Due to the paucity of data, many questions remain regarding the mechanisms by which $Bcl10$ is connected to regulation of actin dynamics. Firstly, it remains unclear whether signaling through the CBM complex is involved, as the RNA silencing studies of Rueda et al. [20] suggest that neither Card11 nor Malt1 are required for TCR-dependent F-actin remodeling in Jurkat T cells. These authors identified TCR-dependent phosphorylation of $Bcl10$ on Ser138 as critical for this activity, and with phosphorylation of Ser138 also being insensitive to Card11 silencing. Thus, the implications of these findings are that Ser138 phosphorylation of $Bcl10$ is TCR-dependent but Card11-independent. Interestingly, Marion et al. [36] demonstrated that blocking phosphorylation of $Bcl10$ at this site via Ser138Ala mutation results in greatly enhanced binding to Card9 (which performs a role functionally similar to Card11 downstream of $Fc\gamma R$ in myeloid cells). Collectively, these data suggest that phosphorylation of Ser138 may redirect $Bcl10$ from CBM complex signaling to regulation of actin cytoskeletal dynamics. As such, the strength of TCR activation may determine the amount of $Bcl10$ available for signaling to NF- κB as a constituent of the CBM complex vs. control of actin cytoskeleton dynamics via a mechanism that requires "free" $Bcl10$. However, such a model would require substantial additional work to validate.

Although we did not investigate CTL function in this study, it is reasonable to postulate that $Bcl10$ -dependent regulation of actin dynamics may influence the efficiency of CTL lysis of target cells. Specifically, Tamzalit et al. [37] recently reported that WASP and Arp2/3 regulate the dynamic formation of actin-rich protrusions in the immunological synapse, which are required for efficient target cell killing. These findings are reminiscent of the above described phagocytic cup data of Marion et al. in the macrophage system, in which a clear $Bcl10$ -dependence was identified. Additionally, given the observations of Rueda et al. showing an impact of $Bcl10$ on TCR-dependent conjugate formation combined with our data showing $Bcl10$ -dependency in regulation of the rate of TCR-stimulated actin flows, CTL interactions with target cells may be altered in the absence of $Bcl10$. Thus, investigation of the relationship between $Bcl10$ expression, actin dynamics, and CTL engagement with and killing of targets is an important area for investigation.

4. Methods

4.1. Cells and reagents

Lymph nodes (LN) and spleens (SPL) were harvested from age-matched 7–12 week old C57BL/6J (WT) mice or $Bcl10^{-/-}$ mice [17] (extensively backcrossed onto a C57BL/6J background). CD8 T cells

were purified from suspensions of mixed LN and SPL cells using a Dynabeads negative selection kit (Invitrogen), followed by differentiation to CD8 effector T cells via 48 hr stimulation with plate-bound anti-TCR and anti-CD28 in EHAA media, followed by culture in IL-2 supplemented media, as described [38,39]. All animal procedures were performed in the USU specific pathogen free animal facility in accordance with the National Research Council's Guide for the Care and Use of Laboratory Animals (The National Academies Press). All animal experiments were approved by the Uniformed Services University (USU) Institutional Animal Care and Use Committee (IACUC) (permit number A3448-01), under protocols MIC-15-575 and MIC-18-575.

pEGFP-C1 F-tractin-EGFP was a gift from Dyche Mullins (Addgene plasmid #58473; <http://n2t.net/addgene:58473>) [24]. The F-tractin-EGFP gene fusion was subcloned from this plasmid into the retroviral vector, pSQZ, consisting of a self-inactivating MSCV backbone, an internal promoter, Qp, which is an Epstein-Barr virus (EBV) constitutive promoter of modest strength [40], and a selectable marker encoding resistance to Zeocin. pSQZ-F-tractin-EGFP was cotransfected with the pCL-Eco packaging plasmid [41] into HEK293T cells to produce ecotropic retrovirus. Viral supernatants were then used to infect differentiating cultures of stimulated murine CD8 T cells, as described [38,39]. Cells expressing F-tractin-EGFP were selected by at least 5 days of growth in EHAA media supplemented with IL-2 and 50 µg/mL Zeocin. The resulting selected populations of CD8 effector T cells were used for imaging experiments in the range of day 7 to day 12 following initiation of anti-TCR/anti-CD28 stimulation.

4.2. Preparation of stimulatory coverslips

8-well chambers (Cellvis, Mountain View, CA) were incubated with a 0.01% solution of poly-L-lysine in distilled water for 10 min at room temperature. The dishes were then dried at 37 °C for 1 h. Poly-L-lysine coated dishes were then incubated with 100 µg/mL mouse anti-TCRβ (clone H57-597, purified from hybridoma supernatant by protein G column chromatography) in 1X-PBS for either 1 h at 37 °C or overnight at 4 °C. The coated chambers were then washed 5 times with Leibovitz's L-15 medium (Fisher Scientific).

4.3. Microscopy

T cells in L-15 medium without serum were seeded on anti-TCRβ coated surfaces equilibrated to 37 °C in a stage-top Okolab Incubator (Okolab S. R. L., Pozzuoli, NA, Italy). We chose to perform experiments without serum in order to obtain reproducible quantitative measurements. The large batch-to-batch variability in FBS could lead to experimental heterogeneity. In addition, serum can block antigen presentation to the T cells, affecting the extent to which plate-bound assays could activate the cells.

Interference reflection microscopy (IRM) and total internal reflection fluorescence (TIRF) images were acquired on an inverted Nikon Ti-E microscope (Nikon, Melville, NY), with 60X and 100X objectives (Nikon, Melville, NY) using a scientific CMOS camera Zyla (Andor, Concord, MA). IRM time-lapse images were acquired every 3 s, while the TIRF images were acquired every 1 s.

4.4. Image analysis

4.4.1. Area calculation from IRM images

In order to calculate the cell area from the IRM images, we first use the *edge* function with the Sobel operator in MATLAB® to detect a threshold based on the intensity gradients. We then tune the threshold value around this initial estimated threshold to obtain a binary mask that is representative of the contours of the cell. This binary image is then dilated and any remaining holes are filled using the *imdilate* and *imfill* functions respectively in MATLAB®. Any connected objects at the boundary are removed using the *imclearborder* function. For datasets

with uneven backgrounds, this approach produced inconsistent segmentation. In these cases, we used *Trainable Weka Segmentation* [42], a machine-learning based segmentation plugin in Fiji [43], in order to segment the IRM images. This approach was validated by comparing the Weka segmentation with the MATLAB®-based segmentation on datasets with uniform illumination.

4.4.2. Edge dynamics

Cell boundaries were extracted using techniques detailed earlier [21]. Briefly, for each frame in the IRM stack, we first low-pass filtered the image to remove shot noise and then corrected for non-uniform illumination. Histograms of the resulting pixel intensities typically exhibited a prominent peak, corresponding to the background, a smaller peak corresponding to tightly adhered regions and a broad tail corresponding to the rest of the cell. Two thresholds were identified by visual inspection to mark the adhered and background pixels. An expectation–maximization algorithm using the thresholds as starting points was used to fit log-concave probability distributions to the background and dark pixels and mark the regions of the image as belonging to the background or the cell (dark and bright pixels, respectively). Dilation operations were used to close the image and obtain a final binary image. An active contour algorithm [44] was applied to perform curvature-driven smoothing of the perimeter of the binary image and any self-intersections were removed. The thresholds were iteratively chosen by comparing computed cell areas in successive images in the time-lapse to minimize large changes. We then used a simplified version of the Machacek-Danuser algorithm [22] while maintaining the basic level set framework to ensure that the computed contours and edge velocities were topologically accurate. First, coarse distance maps, which assign the distance of every grid point from successively sampled cell contours at time t and $t + dt$ were computed using the MATLAB® (Mathworks, Natick, MA) function *bwdist*. A signed distance map was computed from the difference of these two distance functions using the fast marching method [45]. A reinitialization procedure was performed to ensure that the signed distance map remained a true distance function. The resulting distance map is the normal distance from the contour at time t to that at $t + dt$, i.e. the amount that marker points on the contour at t need to be advected by in order to lie on the next contour. We ensured that the Frobenius norm r of the difference between the distance function computed from the advected marker points (the computed contour at $t + dt$) and the original contour at t lay below a fixed threshold. As a cross-check, we verified that the direct solution of the level set PDEs using a 4th order total variation diminishing Runge-Kutta scheme [45] using a speed function computed above yielded similar results to our simplified procedure. The computed normal velocities along the contour were smoothed with a moving window over 10 time points to produce the final velocity maps. The calculated edge velocities were down sampled by averaging along the arc length in blocks of 1 µm (sectors). This length-scale was chosen as it corresponded to the correlation length of the edge dynamics. The velocity time series of each sector was subjected to an empirical mode decomposition followed by a Hilbert-Huang transform in MATLAB® to obtain the instantaneous amplitude and instantaneous frequency distribution of each of the component modes. A maximum of 5 modes were calculated. The instantaneous amplitude values of the second and third modes were pooled across all sectors and all cells for each condition (WT or Bcl10^{-/-}) and compared using the Kolmogorov-Smirnov test.

4.4.3. Actin flow speeds

In order to quantify actin cytoskeletal dynamics, we used STICS to obtain spatiotemporal velocity maps from the fluorescence images. STICS produces a matrix of velocity components, which we use to define a speed and a directional coherence (with respect to the centroid of the cell). The cumulative distribution function of speeds is constructed from speeds of each interrogation window in each time point of the phase. The data from all the cells is compiled into a cumulative

distribution function. The probability density function of directional coherence is similarly defined as a normalized histogram of the individual directional coherences. We used a custom-made MATLAB® script to calculate the cumulative distribution function of the flow speeds from the velocity maps.

4.4.4. Directional coherence

The directional coherence for a region of interest (ROI) with flow velocity \vec{v}_{ij} is defined as

$$\cos\theta_{ij} = \frac{\vec{v}_{ij} \cdot \hat{r}_{ij}}{v_{ij}}$$

where \hat{r}_{ij} is the unit vector pointing from the ROI to the geometric centroid of the cell, and v_{ij} is the flow speed for ROI (i, j) . A directional coherence of +1 indicates a flow moving radially inward and a directional coherence of -1 indicates a flow moving radially outward.

We also defined a metric to quantify the spatial distribution of inward actin flows: the second spatial moment (SSM). We define a flow vector as being “inward” if the directional coherence is larger than 0.8. Once we identify the ROI’s classified as having inward flow, the second spatial moment of the inward flows is defined as:

$$SSM = \frac{1}{NR^2} \sum_{i,j} r_{ij}^2 \cdot \cos\theta_{ij} \cdot H(\cos\theta_{ij} - 0.8)$$

Where N is the total number of ROI’s with a directional coherence larger than 0.8, R is the maximum radius of the cell contact zone, r_{ij} is the distance of the ROI (i, j) from the centroid, $\cos\theta_{ij}$ is the directional coherence, H is the Heaviside function that is defined as:

$$H(x - a) = \begin{cases} 1, & x > a \\ 0, & x \leq a \end{cases}$$

4.4.5. Identification of two temporal phases using k-means clustering

We found that the results for the STICS analysis produced aberrant velocity maps for the first and last time point. In order to prevent these outliers from biasing the clustering analysis, we first exclude these two time points from all analyses. We then use the *kmeans* function in MATLAB® to identify the optimal clusters. Mathematically, the data could be represented by more than two clusters, but we restrict the number of states to two since we qualitatively observe only two distinct states: one with retrograde flow, and one with more disorganized flow. After the state assignment, we correct any time point whose state assignment differs from that of its two nearest (temporal) neighbors. These corrected points tend to lie at the interface of the two clusters, leading to an erroneous state assignment. This is the only user intervention in the process to identify the temporal phases.

5. Data availability

All data supporting the findings of this study are available from the corresponding author upon reasonable request.

CRediT authorship contribution statement

Kaustubh Wagh: Conceptualization, Methodology, Software, Formal analysis, Investigation, Visualization, Writing - original draft. **Brittany A. Wheatley:** Investigation, Writing - review & editing. **Maria K. Traver:** Investigation, Writing - review & editing. **Imran Hussain:** Investigation, Writing - review & editing. **Brian C. Schaefer:** Conceptualization, Investigation, Writing - review & editing, Supervision, Funding acquisition. **Arpita Upadhyaya:** Conceptualization, Formal analysis, Visualization, Writing - original draft, Supervision, Project administration, Funding acquisition.

Declaration of Competing Interest

The authors declare that they have no known competing financial interests or personal relationships that could have appeared to influence the work reported in this paper.

Acknowledgements

This work was supported by the National Institutes of Health (R01 GM131054 to A.U., U01 GM109887 and R01 AI125552 to B.C.S.) and the National Science Foundation (1806903 to A.U.). The authors thank Dr. T. Mak and the University Health Network (UHN), Toronto, CA for *Bcl10*^{-/-} mice.

Appendix A. Supplementary data

Supplementary data to this article can be found online at <https://doi.org/10.1016/j.cellimm.2020.104161>.

References

- [1] O. Acuto, D. Cantrell, T cell activation and the cytoskeleton, *Annu. Rev. Immunol.* 18 (2000) 165–184, <https://doi.org/10.1146/annurev.immunol.18.1.165>.
- [2] M. Huse, The T-cell-receptor signaling network, *J. Cell Sci.* 122 (2009) 1269–1273, <https://doi.org/10.1242/jcs.042762>.
- [3] S. Etienne-Manneville, A. Hall, Rho GTPases in cell biology, *Nature* 420 (2002) 629–635, <https://doi.org/10.1038/nature01148>.
- [4] L. Balagopalan, R.L. Kortum, N.P. Coussens, V.A. Barr, L.E. Samelson, The linker for activation of T cells (LAT) signaling hub: from signaling complexes to microclusters, *J. Biol. Chem.* 290 (2015) 26422–26429, <https://doi.org/10.1074/jbc.R115.665869>.
- [5] D.D. Billadeau, J.C. Nolz, T.S. Gomez, Regulation of T-cell activation by the cytoskeleton, *Nat. Rev. Immunol.* 7 (2007) 131–143, <https://doi.org/10.1038/nri2021>.
- [6] J.K. Burkhardt, E. Carrizosa, M.H. Shaffer, The actin cytoskeleton in T cell activation, *Annu. Rev. Immunol.* 26 (2008) 233–259, <https://doi.org/10.1146/annurev.immunol.26.021607.090347>.
- [7] P. Beemiller, M.F. Krummel, Mediation of T-cell activation by actin meshworks, *Cold Spring Harb. Perspect. Biol.* 2 (2010) a002444, <https://doi.org/10.1101/cshperspect.a002444>.
- [8] K.L. Hui, L. Balagopalan, L.E. Samelson, A. Upadhyaya, Cytoskeletal forces during signaling activation in Jurkat T-cells, *Mol. Biol. Cell.* 26 (2015) 685–695, [https://doi.org/10.1091/mbe.e14-03-0830](https://doi.org/10.1091/mbc.e14-03-0830).
- [9] K. Lam Hui, S.I. Kwak, A. Upadhyaya, Adhesion-dependent modulation of actin dynamics in Jurkat T cells, *Cytoskelet. Hoboken NJ.* 71 (2014) 119–135, <https://doi.org/10.1002/cm.21156>.
- [10] A. Babich, S. Li, R.S. O’Connor, M.C. Milone, B.D. Freedman, J.K. Burkhardt, F-actin polymerization and retrograde flow drive sustained PLCγ1 signaling during T cell activation, *J. Cell Biol.* 197 (2012) 775–787, <https://doi.org/10.1083/jcb.201201018>.
- [11] S. Murugesan, J. Hong, J. Yi, D. Li, J.R. Beach, L. Shao, J. Meinhardt, G. Madison, X. Wu, E. Betzig, J.A. Hammer, Formin-generated actomyosin arcs propel T cell receptor microcluster movement at the immune synapse, *J. Cell Biol.* 215 (2016) 383–399, <https://doi.org/10.1083/jcb.201603080>.
- [12] A. Grakoui, S.K. Bromley, C. Sumen, M.M. Davis, A.S. Shaw, P.M. Allen, M.L. Dustin, The immunological synapse: a molecular machine controlling T cell activation, *Science* 285 (1999) 221–227, <https://doi.org/10.1126/science.285.5425.221>.
- [13] C.R.F. Monks, B.A. Freiberg, H. Kupfer, N. Sciaiki, A. Kupfer, Three-dimensional segregation of supramolecular activation clusters in T cells, *Nature* 395 (1998) 82–86, <https://doi.org/10.1038/25764>.
- [14] M. Thome, J.E. Charlton, C. Pelzer, S. Hailfinger, Antigen receptor signaling to NF-κB via CARMA1, BCL10, and MALT1, *Cold Spring Harb. Perspect. Biol.* 2 (2010) a003004, <https://doi.org/10.1101/cshperspect.a003004>.
- [15] S. Paul, B.C. Schaefer, A new look at T cell receptor signaling to nuclear factor-κB, *Trends Immunol.* 34 (2013) 269–281, <https://doi.org/10.1016/j.it.2013.02.002>.
- [16] T. Gehring, T. Seeholzer, D. Krappmann, BCL10 - bridging CARDs to immune activation, *Front. Immunol.* 9 (2018) 1539, <https://doi.org/10.3389/fimmu.2018.01539>.
- [17] J. Ruland, G.S. Duncan, A. Elia, I. del Barco Barrantes, L. Nguyen, S. Plyte, D.G. Millar, D. Bouchard, A. Wakeham, P.S. Ohashi, T.W. Mak, BCL10 is a positive regulator of antigen receptor-induced activation of NF-κappaB and neural tube closure, *Cell* 104 (2001) 33–42, [https://doi.org/10.1016/s0092-8674\(01\)00189-1](https://doi.org/10.1016/s0092-8674(01)00189-1).
- [18] L.M. Kingeter, B.C. Schaefer, Loss of protein kinase C theta, Bcl10, or Malt1 selectively impairs proliferation and NF-κappaB activation in the CD4+ T cell subset, *J. Immunol. Baltim. Md. 1950* (2008) 6244–6254, <https://doi.org/10.4049/jimmunol.181.9.6244>.
- [19] H.Y. Lu, B.M. Bauman, S. Arjunaraja, B. Dorjbal, J.D. Milner, A.L. Snow, S.E. Turvey, The CBM-opathies—a rapidly expanding spectrum of human inborn

- errors of immunity caused by mutations in the CARD11-BCL10-MALT1 complex, *Front. Immunol.* 9 (2018), <https://doi.org/10.3389/fimmu.2018.02078>.
- [20] D. Rueda, O. Gaide, L. Ho, E. Lewkowicz, F. Niedergang, S. Hailfinger, F. Rebeaud, M. Guzzardi, B. Conne, M. Thelen, J. Delon, U. Ferch, T.W. Mak, J. Ruland, M. Thome, Bcl10 Controls TCR- and FcγR-Induced Actin Polymerization, (n.d.) 13.
- [21] K. Lam Hui, C. Wang, B. Grooman, J. Wayt, A. Upadhyaya, Membrane dynamics correlate with formation of signaling clusters during cell spreading, *Biophys. J.* 102 (2012) 1524–1533, <https://doi.org/10.1016/j.bpj.2012.02.015>.
- [22] M. Machacek, G. Danuser, Morphodynamic profiling of protrusion phenotypes, *Biophys. J.* 90 (2006) 1439–1452, <https://doi.org/10.1529/biophysj.105.070383>.
- [23] X. Ma, O. Dagliyan, K.M. Hahn, G. Danuser, Profiling cellular morphodynamics by spatiotemporal spectrum decomposition, *PLoS Comput. Biol.* 14 (2018) e1006321, <https://doi.org/10.1371/journal.pcbi.1006321>.
- [24] B.J. Belin, L.M. Goins, R.D. Mullins, Comparative analysis of tools for live cell imaging of actin network architecture, *BioArchitecture* 4 (2014) 189–202, <https://doi.org/10.1080/19490992.2014.1047714>.
- [25] H.-G. Döbereiner, B.J. Dubin-Thaler, J.M. Hofman, H.S. Xenias, T.N. Sims, G. Giannone, M.L. Dustin, C.H. Wiggins, M.P. Sheetz, Lateral membrane waves constitute a universal dynamic pattern of motile cells, *Phys. Rev. Lett.* 97 (2006) 038102, <https://doi.org/10.1103/PhysRevLett.97.038102>.
- [26] A.T. Ritter, S.M. Kapnick, S. Murugesan, P.L. Schwartzberg, G.M. Griffiths, J. Lippincott-Schwartz, Cortical actin recovery at the immunological synapse leads to termination of lytic granule secretion in cytotoxic T lymphocytes, *Proc. Natl. Acad. Sci. USA.* 114 (2017) E6585–E6594, <https://doi.org/10.1073/pnas.1710751114>.
- [27] S. Kumari, D. Depoil, R. Martinelli, E. Judokusumo, G. Carmona, F.B. Gertler, L.C. Kam, C.V. Carman, J.K. Burkhardt, D.J. Irvine, M.L. Dustin, Actin foci facilitate activation of the phospholipase C-γ in primary T lymphocytes via the WASP pathway, *eLife* 4 (2015), <https://doi.org/10.7554/elife.04953>.
- [28] M. Fritzsche, R.A. Fernandes, V.T. Chang, H. Colin-York, M.P. Clausen, J.H. Felce, S. Galiani, C. Erlenkämper, A.M. Santos, J.M. Heddleston, I. Pedroza-Pacheco, D. Waithe, J.B. de la Serna, B.C. Lagerholm, T.-L. Liu, T.-L. Chew, E. Betzig, S.J. Davis, C. Eggeling, Cytoskeletal actin dynamics shape a ramifying actin network underpinning immunological synapse formation, *Sci. Adv.* 3 (2017) e1603032, <https://doi.org/10.1126/sciadv.1603032>.
- [29] H. Colin-York, S. Kumari, L. Barbieri, L. Cordes, M. Fritzsche, Distinct actin cytoskeleton behaviour in primary and immortalised T-cells, *J. Cell Sci.* 133 (2019), <https://doi.org/10.1242/jcs.232322>.
- [30] B. Hebert, S. Costantino, P.W. Wiseman, Spatiotemporal image correlation spectroscopy (STICS) theory, verification, and application to protein velocity mapping in living CHO cells, *Biophys. J.* 88 (2005) 3601–3614, <https://doi.org/10.1529/biophysj.104.054874>.
- [31] S. Lloyd, Least squares quantization in PCM, *IEEE Trans. Inf. Theory.* 28 (1982) 129–137, <https://doi.org/10.1109/TIT.1982.1056489>.
- [32] J. Yi, X.S. Wu, T. Crites, J.A. Hammer, T.D. Pollard, Actin retrograde flow and actomyosin II arc contraction drive receptor cluster dynamics at the immunological synapse in Jurkat T cells, *Mol. Biol. Cell.* 23 (2012) 834–852, [https://doi.org/10.1091/mbe.e11-08-0731](https://doi.org/10.1091/mbc.e11-08-0731).
- [33] I. Rey-Suarez, B.A. Wheatley, P. Koo, A. Bhanja, Z. Shu, S. Mochrie, W. Song, H. Shroff, A. Upadhyaya, WASP family proteins regulate the mobility of the B cell receptor during signaling activation, *Nat. Commun.* 11 (2020) 439, <https://doi.org/10.1038/s41467-020-14335-8>.
- [34] O. Gaide, B. Favier, D.F. Legler, D. Bonnet, B. Brissoni, S. Valitutti, C. Bron, J. Tschopp, M. Thome, CARMA1 is a critical lipid raft-associated regulator of TCR-induced NF-κB activation, *Nat. Immunol.* 3 (2002) 836–843, <https://doi.org/10.1038/ni830>.
- [35] B.C. Schaefer, J.W. Kappler, A. Kupfer, P. Marrack, Complex and dynamic redistribution of NF-κB signaling intermediates in response to T cell receptor stimulation, *Proc. Natl. Acad. Sci.* 101 (2004) 1004–1009, <https://doi.org/10.1073/pnas.0307858100>.
- [36] S. Marion, J. Mazzolini, F. Herit, P. Bourdoncle, N. Kambou-Pene, S. Hailfinger, M. Sachse, J. Ruland, A. Benmerah, A. Echard, M. Thome, F. Niedergang, The NF-κB signaling protein Bcl10 regulates actin dynamics by controlling AP1 and OCRL-bearing vesicles, *Dev. Cell.* 23 (2012) 954–967, <https://doi.org/10.1016/j.devcel.2012.09.021>.
- [37] F. Tamzalit, M.S. Wang, W. Jin, M. Tello-Lafoz, V. Boyko, J.M. Heddleston, C.T. Black, L.C. Kam, M. Huse, Interfacial actin protrusions mechanically enhance killing by cytotoxic T cells, *Sci. Immunol.* 4 (2019), <https://doi.org/10.1126/sciimmunol.aav5445>.
- [38] M.K. Traver, S. Paul, B.C. Schaefer, T cell receptor activation of NF-κB in effector T cells: visualizing signaling events within and beyond the cytoplasmic domain of the immunological synapse, *Methods Mol. Biol.* Clifton NJ. 1584 (2017) 101–127, https://doi.org/10.1007/978-1-4939-6881-7_8.
- [39] S. Paul, B.C. Schaefer, Visualizing TCR-induced POLKADOTS formation and NF-κB activation in the D10 T-cell clone and mouse primary effector T cells, *Methods Mol. Biol.* Clifton NJ. 1280 (2015) 219–238, https://doi.org/10.1007/978-1-4939-2422-6_12.
- [40] B.C. Schaefer, J.L. Strominger, S.H. Speck, Redefining the Epstein-Barr virus-encoded nuclear antigen EBNA-1 gene promoter and transcription initiation site in group I Burkitt lymphoma cell lines, *Proc. Natl. Acad. Sci. USA* 92 (1995) 10565–10569, <https://doi.org/10.1073/pnas.92.23.10565>.
- [41] R.K. Naviaux, E. Costanzi, M. Haas, I.M. Verma, The pCL vector system: rapid production of helper-free, high-titer, recombinant retroviruses, *J. Virol.* 70 (1996) 5701–5705.
- [42] I. Arganda-Carreras, V. Kaynig, C. Rueden, K.W. Eliceiri, J. Schindelin, A. Cardona, H. Sebastian Seung, Trainable weka segmentation: a machine learning tool for microscopy pixel classification, *Bioinformatics.* 33 (2017) 2424–2426, <https://doi.org/10.1093/bioinformatics/btx180>.
- [43] J. Schindelin, I. Arganda-Carreras, E. Frise, V. Kaynig, M. Longair, T. Pietzsch, S. Preibisch, C. Rueden, S. Saalfeld, B. Schmid, J.-Y. Tinevez, D.J. White, V. Hartenstein, K. Eliceiri, P. Tomancak, A. Cardona, Fiji: an open-source platform for biological-image analysis, *Nat. Methods* 9 (2012) 676–682, <https://doi.org/10.1038/nmeth.2019>.
- [44] X.u. Chenyang, J.L. Prince, Gradient vector flow: a new external force for snakes, *Proc. IEEE Comput. Soc. Conf. Comput. Vis. Pattern Recognit., IEEE Comput. Soc.* San Juan, Puerto Rico (1997) 66–71, <https://doi.org/10.1109/CVPR.1997.609299>.
- [45] S. Osher, R. Fedkiw, *Level Set Methods and Dynamic Implicit Surfaces*, Springer, New York, 2003.